

## The STIS CCD Spectroscopic Line Spread Functions<sup>1</sup>

T. Gull, D. Lindler<sup>2</sup>, D. Tennant<sup>3</sup>, C. Bowers, C. Grady<sup>4</sup>, R. S. Hill<sup>5</sup>, and E. Malumuth<sup>5</sup>

*Laboratory for Astronomy and Solar Physics, Code 681, NASA's Goddard Space Flight Center, Greenbelt, MD, 20771*

**Abstract.** We characterize the spectroscopic line spread functions of the spectroscopic CCD modes for high contrast objects. Our long range goal is to develop tools that accurately extract spectroscopic information of faint, point or extended sources in the vicinity of bright, point sources at separations approaching the realizable angular limits of HST with STIS. Diffracted and scattered light due to the HST optics, and scattered light effects within the STIS are addressed. Filter fringing, CCD fringing, window reflections, and scattering within the detector and other effects are noted. We have obtained spectra of several reference stars, used for flux calibration or for coronagraphic standards, that have spectral distributions ranging from very red to very blue. Spectra of each star were recorded with the star in the aperture and with the star blocked by either the F1 or F2 fiducial. Plots of the detected starlight along the spatial axis of the aperture are provided for four stars. With the star in the aperture, the line spread function is quite noticeable. Placing the star behind one of the fiducials cuts the scattered light and the diffracted light is detectable even out to 10000Å. When the star is placed behind either fiducial, the scattered and diffracted light components, at three arcseconds displacement from the star, are below  $10^{-6}$  the peak of the star at wavelengths below 6000Å; at the same angular distance, scattered light does contaminate the background longward of 6000Å up to a level of  $10^{-5}$ .

### 1. Introduction

The distinctive advantages of Hubble Space Telescope (HST) are near-diffraction-limited imaging performance and access to the ultraviolet. The Space Telescope Imaging Spectrograph (STIS), as its name states, takes advantage of the near-diffraction-limited capability of HST and provides spectral dispersions ranging from  $R \simeq 500$  and 10,000 from 1175 - 10,000 Å and  $\simeq 30,000$  to 180,000 from 1175 to 3200Å. The optical design and detector performance of STIS was carefully matched to science problems that the STIS Instrument Development Team (IDT) realized could be addressed with high angular resolution and selected spectral dispersions. We designed the detector formats to utilize the angular resolution of the pri-

---

<sup>1</sup>Based upon observations with the NASA/ESA Hubble Space Telescope, obtained at the Space Telescope Science Institute, which is operated by the Association of Universities for Research in Astronomy, Inc., under NASA contract, NAS 5-26555.

<sup>2</sup>Advanced Computer Concepts

<sup>3</sup>Naval Academy

<sup>5</sup>Science Systems Applications, Inc.

<sup>4</sup>National Optical Astronomy Observatory

mary optics. For the CCD modes (1650-10,000Å,  $R \simeq 500$  and 10,000), the pixel sampling is  $0''.0504$ . In keeping with the philosophy of developing the second generation of instruments for HST, state-of-the-art detector technology was pushed to obtain the best detectors possible for space observations and numerous spectral modes were installed to provide a range of resolving powers.<sup>1</sup> Late in testing of the CCD modes, we realized that increased transparency in the near red of the silicon bulk material led to increased internal scatter within the detector and support substrate. This red scatter would complicate spectroscopy, direct imagery and especially coronagraphic imagery done with the STIS CCD.

Success of HST with STIS is measurable in many ways. With each cycle of competition for HST observational time, proposals to use the STIS have been quite successful. We point to the successful measurements of black hole masses in the nuclei of many galaxies, and more recently at the cores of globular clusters, of the spectroscopic transit of a planet across the surface of a distant star, of the lack of planets in globular clusters, of measurements of the Gunn-Peterson effect and of the Lyman alpha forests, of the first ultraviolet spectra of gamma ray bursters, and of nebular structures in very close vicinity to bright stars. The HST/STIS has broken many barriers to ground-based spectroscopy, yet data reduction and analysis continues to be challenging when we attempt to pull out weak, extended structures close to a bright central source. As we have learned more and more about the performance of STIS, we have felt encouraged to push the limits of its capabilities. In this discussion, we present some measures of the line spread function for the CCD spectroscopic modes as a function of wavelength. In the future, we hope that software will be developed to enable all users to take full advantage of the remarkable rejection that STIS provides off axis. More importantly, we hope that this information on the realized performance of STIS will provide insights for improved instrument performance of future ground-based and especially space-based instruments.

For the HST/STIS user, many observations can be accomplished routinely. If two objects are at the classical separation (one full at half maximum separation), then the data reduction/analysis is relatively straightforward. Here we address optical performance that must be taken into account when the relative intensities are  $> 20$ . With the potential of reaching statistical  $S/N > 20$ , large contrast factors can be addressed. In short this discussion is in the very important application when a very low extended source, or even a faint point source, is detectable near a significantly brighter, point source.

## 2. Examples of a STIS CCD High Contrast Observations

We start with a spectrum of a K0 star (HD181204) dispersed by the G750L grating from 5000 to 10,000Å (Figure 1). The top and middle spectra display the same spectrum with relative flux scales of 100. The bottom spectrum is of the same star behind the F1 ( $0''.5$ ) fiducial<sup>2</sup> which blocks the core light by nearly four orders of magnitude. The grey scale for the bottom spectrum is 1/300th that of the top spectrum. Longward of 7000Å, the

---

<sup>1</sup>Dr. James Milligan, while an enthusiastic supporter of the STIS, as chair of the Flight Readiness Review noted that STIS was the most complicated spacecraft he had ever reviewed . . . and that it was only an instrument. That STIS has performed to specification and exceeded the five year lifetime (and we hope it continues to perform excellently to the end of the HST mission) is a tribute to the STIS IDT, the engineering staff and the STScI STIS team that made it happen and keep it operational!

<sup>2</sup>The STIS has an aperture wheel that allows for a selection of optimized apertures to fit the desired scientific observation. An internal calibration system (WAVECAL) feeds light from a Pt(Cr) lamp to provide reference wavelengths for wavelength and velocity measures. Positional information is defined by two fiducials (F1, which is  $0''.5$  wide, and F2, which is  $0''.8$  wide) on each long aperture. The aperture wheel encoding permits very precise placement of the apertures, sufficiently accurate in position, that a stellar image can be blocked by rotating the aperture into position. The fiducial tests in this paper were performed with the  $52'' \times 0''.2$  and the  $52'' \times 0''.1$  apertures.

silicon structure of the CCD absorbs less radiation, and the light is reflected within the chip structures. Diffuse scattering becomes increasingly apparent with wavelength and spreads across the CCD. The CCD in the near-red behaves much like a Fabry-Perot interferometer, and develops wavelength-dependent fringes in response to the dispersed light. Properly executed flat fields can be used to correct the fringed response for objects positioned within the aperture. Recently, Malumuth et al. (2002) developed a calibration scheme for objective grating spectra of objects in the STIS CCD parallel modes (see also Malumuth et al., these proceedings). The fringes seen in the bottom image of Figure 1 are not CCD-induced fringes, but the classical fringes due to diffraction of the telescope optics. In a perfect spectrograph, these fringes would be the limiting factor in observing faint sources in the vicinity.

The collapsed Line Spread Function (LSF) is plotted in Figure 2 for the same spectra of the star imaged in Figure 1. The upper trace is of the unobstructed star LSF sampled through the  $52'' \times 0''.2$  aperture. The middle trace is of the same star, HD181204, placed behind the F1 fiducial ( $0''.5$  wide) and the bottom trace is with the star placed behind the F2 fiducial ( $0''.8$  wide). The fiducial cuts the wings of the LSF by  $10^2$ . We note that this spectral LSF is a linear approximation of a much more complex function. In the stellar spectrum spread horizontally across the two-dimensional CCD, each wavelength has a scattering function that spreads in two dimensions. The narrow aperture at the entrance to the STIS cuts the PSF of HST to a thin slice that is then modified by each optical element. In the ideal situation, this modification would simply be the spectral separation of the input light. However each optical element can contribute scatter or modulation to the light, creating a PSF response that is wavelength dependent. We find that the major effect is light scattering in the CCD detector itself and that the scattering becomes more pronounced to the red part of the spectrum. However to get reasonable S/N measures of the LSF, we had to collapse the data in the spectral direction to measure the LSF along the cross-dispersion, the angular or the spatial direction. The reader is cautioned that a wavelength LSF is needed, especially at wavelengths longward of  $7000\text{\AA}$ . Between  $3000$  and  $7000\text{\AA}$ , an averaged LSF, scaled with wavelength due to HST optics diffraction effects likely will suffice.

Scattered light is a major problem for faint, extended or complex structures along the aperture. Eta Carinae, with the Homunculus (a bi-lobed nebula plus disk system of ejecta) is one such complex structure with scales well matched to the angular resolution of HST. Most of the nebula is a reflection nebula shell with some ionized metals, but neutral hydrogen. Close to the star is a series of emission structures, including a Little Homunculus (Ishibashi, et al. 2002). Figure 3 shows an extracted portion of three spectra including Balmer alpha (G750M, centered on  $6768\text{\AA}$ ). Eta Carinae is centered within the  $52'' \times 0.1''$  aperture in the lower spectrum. In the logarithmic stretch across five decades, a faint ghost is noticeable to the lower right of the bright, broadened Balmer alpha emission profile of the star. Faint nebular emission consisting of narrow Balmer alpha and [N II], [S II] emission lines can be seen, but the brightness is only slightly above the video pickup, with  $\simeq 4DN$  amplitude. The middle and top spectra were recorded with the  $52'' \times 0.2''$  aperture, but with the F2 ( $0.8''$  width) fiducial rotated to block the star. The middle spectrum (10 seconds CR-SPLIT) brings out the nebular emission lines well above the video pickup, and the scattered starlight continuum can be seen, including the broad Balmer alpha emission, complete with a nebular absorption line. Some video pickup is noticeable. The top spectrum (150 seconds CR-SPLIT) goes very deep, but some of the scattered Balmer alpha emission has saturated at the edge of the fiducial and is bleeding into the nebular portion of the spectrum. Closer inspection of this spectrum pulls out over twenty unique narrow nebular emission lines, two of which are [Sr II] detected for the first time (Zethson, et al. 2000).

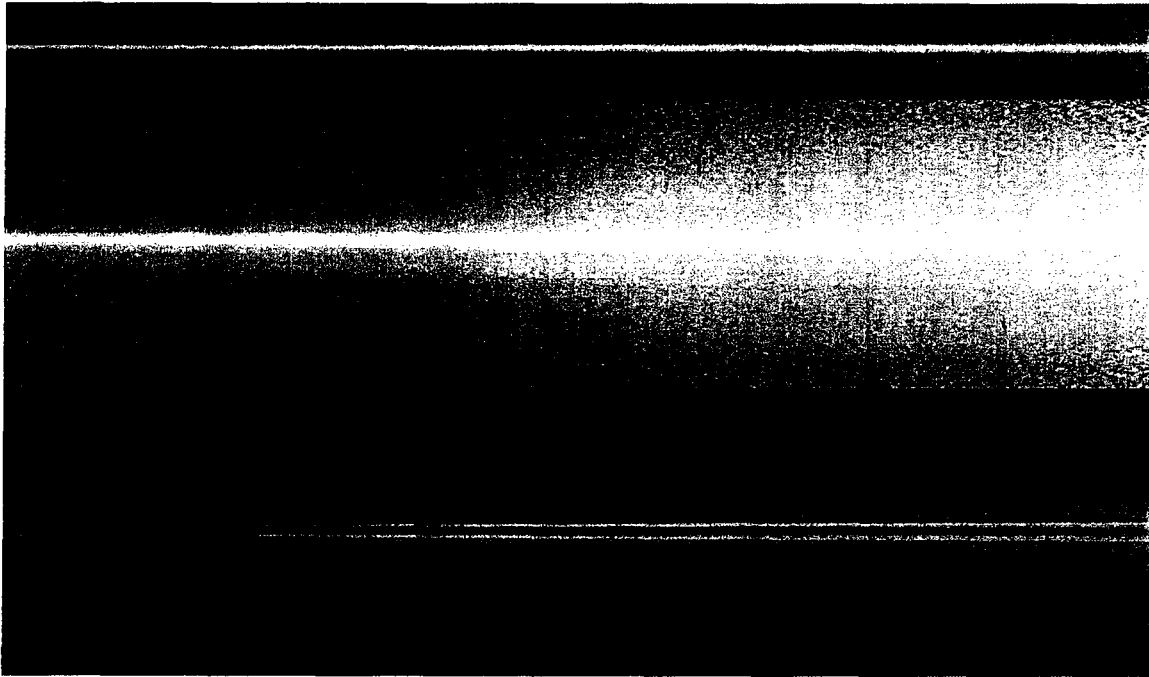


Figure 1. Spectra of HD181204 (MIII) from 5000 to 10,000Å through the 52''x 0.2 STIS aperture. The top and middle spectra are the same spectrum, but with a grey scale change of  $10^2$ . The bottom spectrum is with the star placed behind the F1 fiducial (0.5 wide), displayed with a grey scale 1/300th that of the top spectrum. The HST diffracted light pattern is now visible.

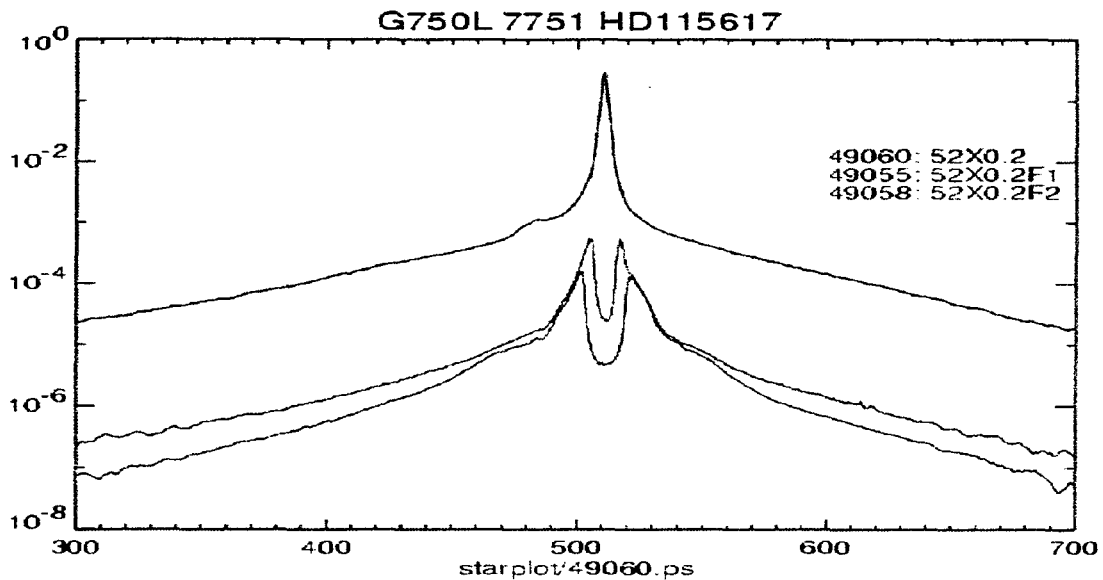


Figure 2. Collapsed Line Spread Function (LSF) for G750L (5000 to 10,000Å) of the HD181204 (MIII) (Figure 1). The upper trace is the LSF for the unobstructed spectrum. The middle trace is the LSF for the star placed behind the F1 (0.5 wide). The bottom curve is the LSF for the star placed behind the F2 (0.8 wide).

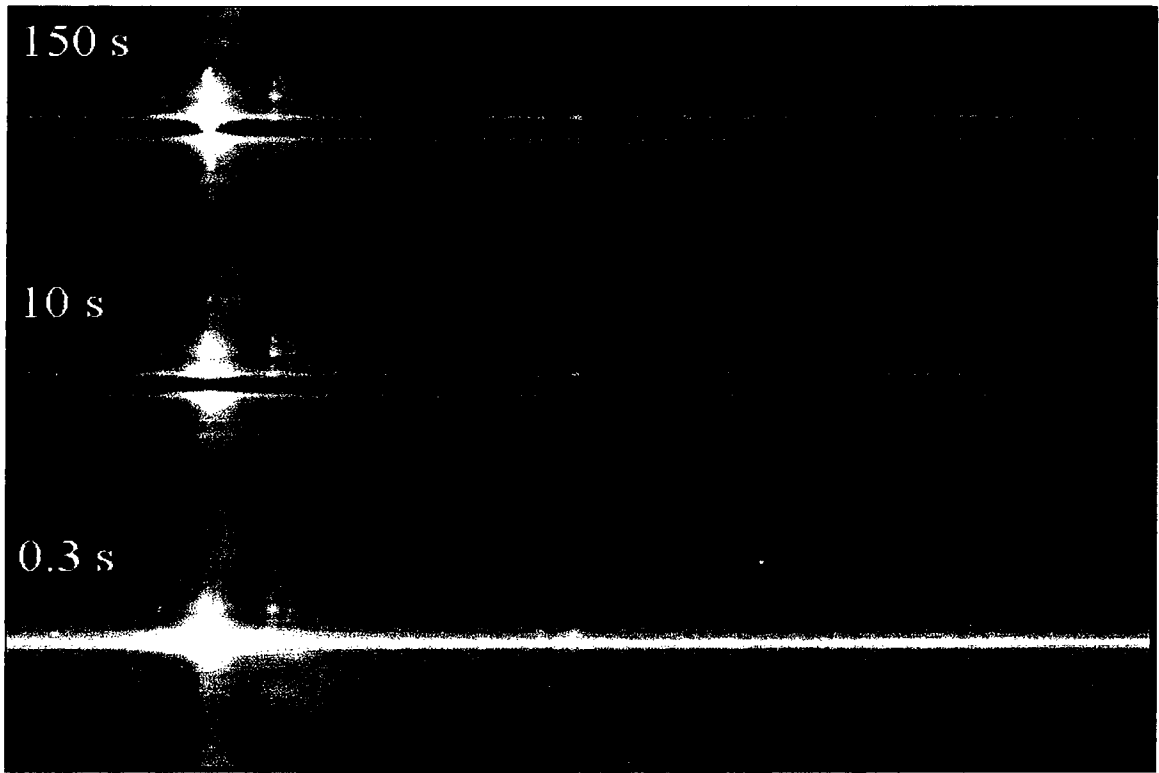


Figure 3. Spectra of Eta Carinae and Very Nearby Ejecta from 6400 to 7000Å. All three spectra are plotted with a dynamic log scale of  $10^5$ . The bottom spectrum includes Eta Carina in the  $52'' \times 0.1''$  aperture for an exposure time of 0.3 seconds. Note the broad, diffuse structure to the right and just below the Balmer alpha P-Cygni emission line. This is a ghost image of the bright Balmer alpha line due to reflections off the CCD detector housing. The middle spectrum is with the  $52'' \times 0.2''$  aperture, but with Eta Carinae behind the F2 ( $0.8''$ ) fiducial and is a 10 second CR-SPLIT exposure. The top spectrum is similar to the middle spectrum, but with a 150 second, CR-SPLIT=2 exposure. The brightest line, Balmer alpha from the star and scattered by the immediate nebulosity, spills over the fiducial into the extended nebula. In the top frame, Balmer alpha is some pixels in the y-column. Each of the three spectra are a slice extending plus and minus two '' from Eta Carinae approximately along the bipolar axis of symmetry. The ghost, seen in the spectrum when the star is centered in the aperture, is greatly decreased as the very bright emission line from the star is blocked by the fiducials in the middle and top tracings.

### 3. Known Limitations

As with any spectrograph, each optical element utilized in the optical train alters the output. Some changes are not desirable, whether they are diffraction effects, scattered light, faint reflections at every transmitting surface, stray light, or detector performance. The challenge is to anticipate these problems and to minimize deleterious effects on the product. STIS is no exception, and as shown in this paper, we are pushing the instrument capabilities to the realizable limits. Indeed one major reason for preparing this paper is to document the realized instrument capabilities and to sensitize designers of future spectrographs to shortcomings that must be overcome if astronomers wish to study complex systems with even higher contrasts.

Each first order grating has a blocking filter to ensure no second order (blue) leakage contaminates first order spectra at the red end. Each blocking filter is attached directly to the grating mount. Collimated light passes through these filters both in the incident and diffracted beam. A small modulation is detectable especially in the spectra of calibration emission lamps where the  $f$ /ratio of the optical system is very large and the intrinsic line widths are much narrower than the resolving power of the spectrograph ( $R \approx 500 - 10,000$ ). For astronomical continuum sources the modulation is significantly less than a percent and for emission line sources, the modulation would be a few percent for intrinsic linewidths approximately 20km/s. Spectroscopy of NGC7009 yielded a measured peak-to-peak modulation of 3 % for the ratio of [O III] 5007Å/ 4959Å (Rubin, et al. 2001).

The ghost image, noted in Figure 3, is of much greater concern. Direct images, as exemplified in Figure 4, show a faint double ring to one side of each bright star image. The position of these rings relative to the star image moves, depending upon the position of the star on the detector. R. S. Hill (2000, 2001) analyzed many direct and spectroscopic images recorded by STIS (Figures 4,6 and 7). In the red, the integrated flux of the double rings is a few percent of the total flux of the star. Figure 8 is a diagram showing the path traced by the principal ray impinging upon the CCD. The CCD surface reflects the focused image, at  $f/48$ , back to the fused silica housing window (necessary to prevent contamination accumulating on the CCD surface!). Reflections from both window surfaces result in the two out of focus, displaced images next to each star in Figure 4. Hill's report (2000) demonstrates that the rings on direct images are well behaved. Lines, extending through each stellar and associated pair of ghost images, come to a common region on the detector. Figure 5 reproduces his measures of the positional displacements). The dispersed spectrum of a star, shown in Figure 6, demonstrates that the double rings build up a shoulder offset below the stellar spectrum. The integrated amplitude, which changes with wavelength, is a few percent of the total stellar flux in the red, but nearly negligible in the 2000-3000Å spectral region as an antireflection coating was placed on the window for the blue portion of the spectrum.

Quite a different response is noted for WAVECAL spectra (Figure 7). The double ring phenomenon is not present, but a series of fringes in the approximate positions, expected for the the CCD window ghosts, are seen. We were puzzled about this difference until recently. A two orbit spectrum of the brightest portion of the Orion nebula was recorded of Balmer Alpha (6563Å) and [N II] (6548Å and 6584Å). No fringes were observed at the expected ghost positions. The twelve sub-exposures were combined together by CALSTIS using the cosmic-ray rejection algorithm. Detection of the ghost is very marginal as the relative brightness per pixel is  $\approx 10^{-4}$  that of the peak emission line brightness. However, measures of the fringe amplitudes on the WAVECAL exposures are closer to  $\approx 10^{-3}$  of the peak emission line brightnesses. We realized that the WAVECALs were done through a slightly different optical train in front of the STIS aperture, designed to minimize usage of the STIS shutter/calibration mirror mechanism.

Lifetime of a mechanism in a space instrument is always a concern. A shutter moves in and out of the input light path to prevent light from entering during an exposure and

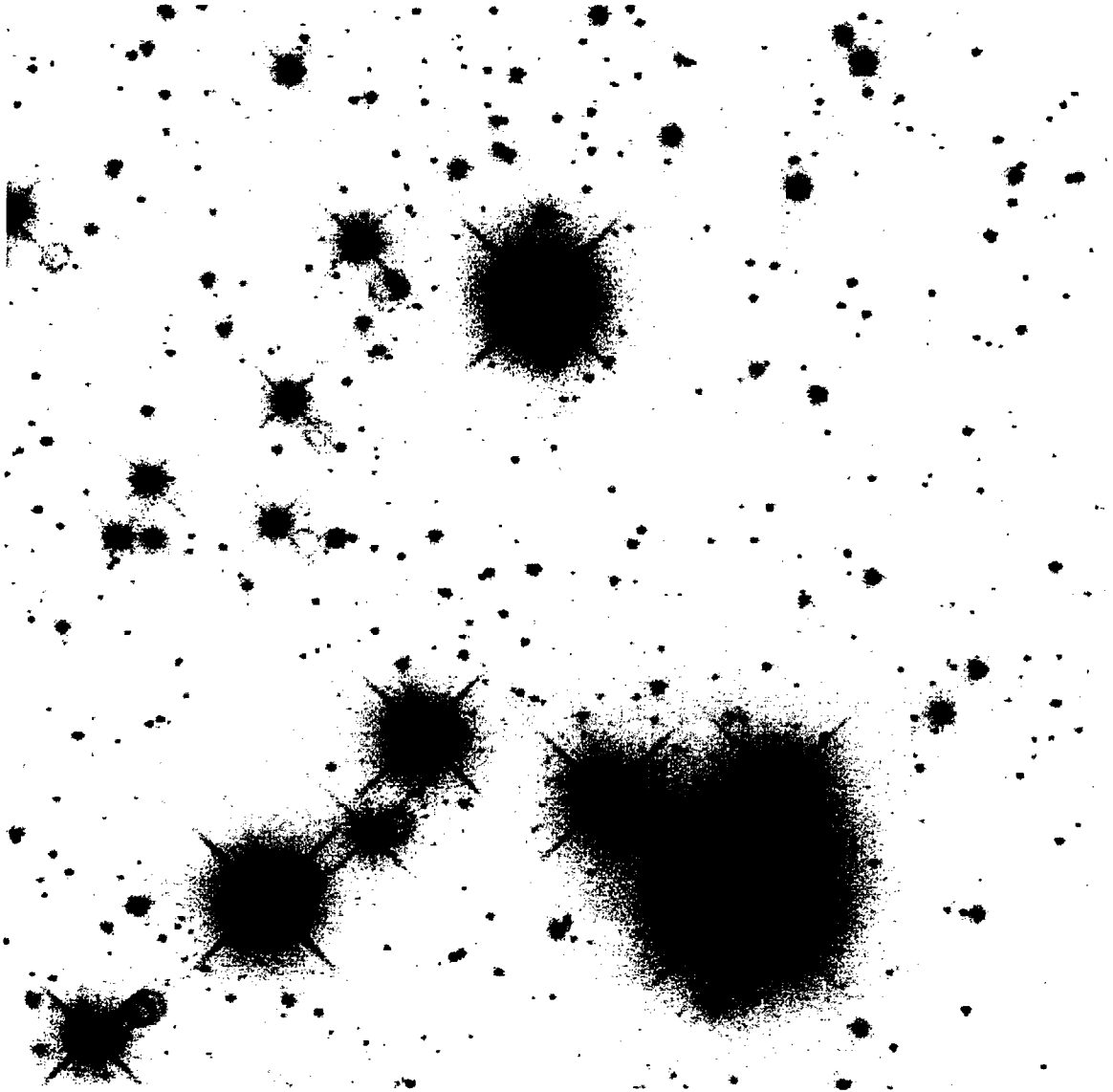


Figure 4. Broad-Band Direct Image Recorded by the STIS CCD. Each stellar image has two ghost rings due to reflections off of the CCD detector housing window. Note that the reflections relative to the stellar position move about a point. This is due to the pupil plane being a significant distance behind the detector plane (See figures 5 through 8).

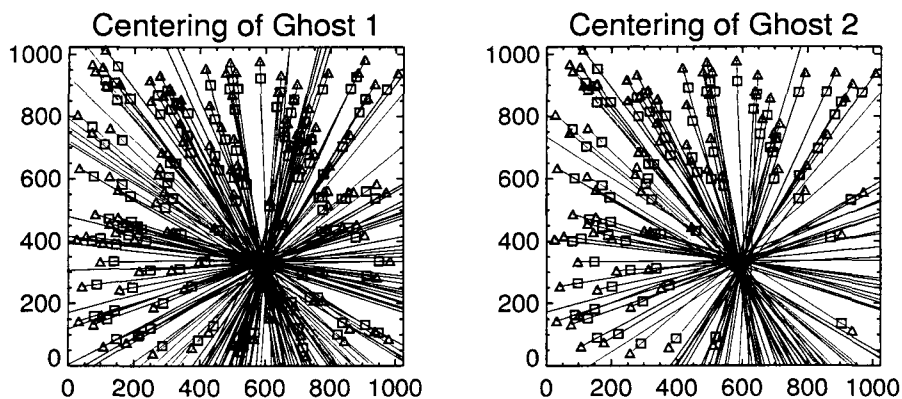


Figure 5. Centering of the Two Ghosts within the CCD Detector Format. A line, drawn through the stellar image and the centers of one of the ghosts, extends to a common region on the CCD format. With the spectrum dispersed across in row 511, the ghost is BELOW the spectrum. Were the spectrum placed in row 100, the ghost would appear ABOVE the spectrum.

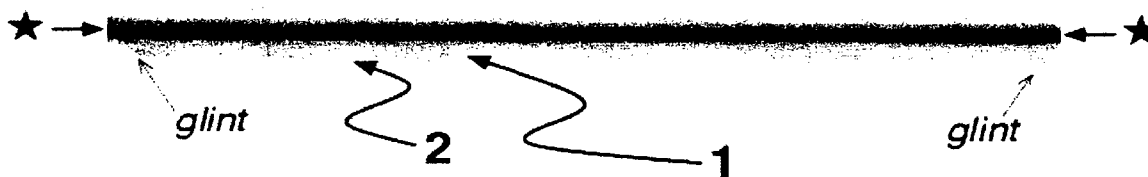


Figure 6. Stellar spectrum with the Ghost Window Reflection. The integrated flux in the ghost is a few percent of the stellar flux, but is over an extended number of pixels. Typical amplitudes per pixel are a few parts in  $10^4$  of the peak stellar amplitude.

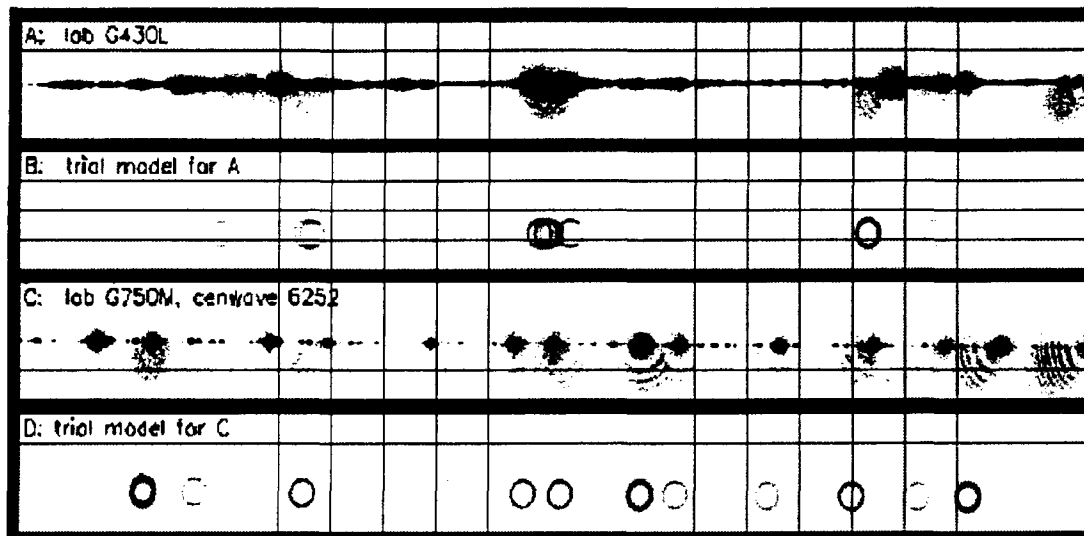


Figure 7. Sample Calibration Spectra and Simulations. External and internal lamp calibrations taken before launch demonstrate that the ghost position shifts with respect to the line position along the x-axis and that the internal hole-in-the-mirror (HITM) calibration ghosts are fringed. We have since realized this is due to the very large focal ratio of the HITM optical system, and not of the  $f/24$  optical beam from the telescope.

to prevent light contamination by STIS of any other instrument operating in parallel. The backside of the shutter has a mirror that feeds light into the instrument for LAMP calibrations. To minimize the movement of the shutter, an alternate light path was developed to feed light from the calibration optical train through a permanently mounted mirror and a hole in the second relay mirror (the relay mirrors correct for the optical aberrations of HST), and to illuminate the STIS aperture. This mode is labelled HITM (hole in the mirror . . . what else?) and is well within the shadow of the HST secondary. Thus the HITM mode is feeding light from an emission line lamp with a very large  $f$ /ratio into STIS. The intrinsic line widths are far narrower than the spectral resolving power of the first order gratings. The reflected light off of the two surfaces of the detector window becomes modulated as the light paths are sufficiently different and tilted relative to the incident light beam. We are unable to detect the extremely narrow modulation of the continuum sources, lamp or stellar, because the wavelength variation is continuous and hence we see the rings instead of fringes. One simple test to confirm this was a comparison of a LAMP spectrum to a HITM spectrum. The LAMP mode overfills the relay optics, ensuring a light beam comparable to the  $f/24$  beam of the telescope. The fringing of the LAMP spectrum for the Pt(Cr) lamp spectra is noticeably less than the HITM spectrum. As nearly all astronomical sources have intrinsic line widths (thermal plus turbulence plus multiple components) the fringing is negligible.

#### 4. Spectroscopic LSF Observations

To characterize the faint scattering characteristics of STIS, spectroscopic LSF measurements were done of stars placed within a long aperture and then blocked by a fiducial. Indeed, we realized that characterization of coronagraphic imagery (see Grady, et al. this conference proceedings) could be enhanced by these spectroscopic measurements. The HST point

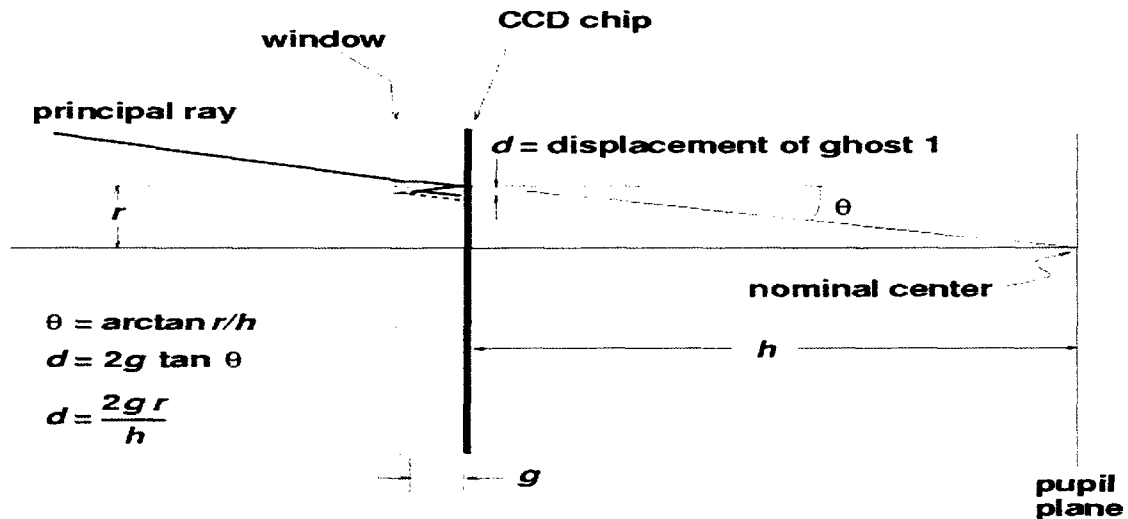


Figure 8. Optical Paths of the Incident Light and the Reflected Light. The ghost images are displaced from the primary spot due to the pupil plane being at a significant distance behind the detector surface.

spread function for a star is a weighted function of the spectral distribution. For a well-behaved panchromatic detector, the HST/STIS response would be expected to be spectral distribution of a known star weighted by the diffraction-limited HST PSF and sampled by the selected STIS entrance aperture. However, the STIS CCD has a very significant scattering component longward of  $7000\text{\AA}$  as demonstrated in Figures 1 and 3. Our desire to quantify the detector scattering component and to understand the effects on observations led to requesting stellar measurements performed with proposal 8844.

We selected four stars, which were thought to be point-like with respect to HST's angular resolving power. Other criteria were that there be no measurable infrared excess (suggesting possible dust and gas surrounding the star); that the stars be bright enough to be able to record spectra of the star in a few seconds and to be able to record the scattered light passed by the STIS aperture fiducials F1 ( $0''.5$ ) and F2 ( $0''.8$ ); that the star not be in a crowded field to minimize confusion; and that the star be easily accessible, namely close to the orbital pole if possible. STIS has an aperture wheel with approximately fifty preformed apertures. As the selected aperture is moved into the light path and the selected grating (also on a wheel) is moved into the light path, an efficient method was devised to quickly determine the spectral position on the detector. The emission line calibration source, as noted above, feeds into the corrector/relay optics and through the instrument to the detector. A WAVECAL is recorded without the internal optics being moved before the astronomical source is observed. In line identifications of the Weigelt blob B and D, located close to Eta Carinae, Zethson (2000) found that the wavelengths were accurate to about one-fifth of a STIS CCD pixel, based upon measured versus laboratory wavelengths of nearly 2500 emission lines. Position along any long aperture is referenced by two fiducials placed at some distance above and below the aperture center. As the aperture wheel is very finely encoded, the aperture rotation can be defined to place either the F1 or the F2 fiducial to obscure the stellar image. Currently only the F2 fiducial position for the  $52'' \times 0''.2$  aperture is supported for routine observations. However other fiducials have been used. In proposal 8844, we used the F1 and F2 fiducials for both the  $52'' \times 0''.2$  and the  $52'' \times 0''.1$  apertures with excellent success.

The most pressing criterion listed above was the desire to observe these stars in a reasonable number of orbits. As a barebones minimum, we chose to use all three low dispersion gratings: G750L (5000 to 10,000Å), G430L (3000 to 5000Å) and G230LB (1600 to 3100Å). As there are approximately forty primary settings for the M gratings, only the most frequently used M-mode settings were tested: G750M (8561Å and 6768Å), G430M (4961Å and 3936Å) and G230MB (2836Å). Most grating settings were used with the A0V star, HD141653, as the exposure times were reasonable and much could be learned throughout the spectrum. Only a subset of grating settings were used in the blue for the B+75D325 (WD) and in the red for HD115617 (GV) and HD181204(MIII). The observed combinations are listed in Table 1. The WD, BD+75D325, was selected because it is a primary standard used in monitoring the sensitivity of STIS. The other three stars were selected because they had proved to be excellent reference stars for STIS coronagraphic observations (Grady, this conference) and because they spanned the spectral types from MIII to GV to A0V. Initially, we thought that the reference PSF of stars of intermediate spectral types could be modelled by a weighted combination of the PSF's measured for these stars. However, the best reference PSF's are those of similar stars taken during orbits immediately before or after the stars of interest because thermally induced collimation and focus changes are of greater impact.

Table 1. Stars Observed in Proposal 8844 for this Study

| Star      | SpT  | APER   | G750L   | G750M        | G430L   | G430M        | G230LB  | G230MB |
|-----------|------|--------|---------|--------------|---------|--------------|---------|--------|
| BD+75D325 | WD   | 52X0.2 | -       | -            | A,F1,F2 | A,F1 4961    | A,F1,F2 | A 2836 |
| HD141653  | A0V  | 52X0.2 | A,F1,F2 | A,F1 6768    | A,F1,F2 | -            | A,F1,F2 | -      |
| "         | "    | 52X0.2 | -       | A,F1,F2 8561 | -       | A,F1,F2 3936 | -       | -      |
| "         | "    | 52X0.1 | -       | A,F1,F2 8561 | -       | A,F1,F2 4961 | -       | -      |
| HD115617  | GV   | 52X0.2 | A,F1,F2 | A,F1,F2 6768 | A,F1,F2 | -            | A,F1,F2 | -      |
| HD181204  | MIII | 52X0.2 | A,F1,F2 | A,F1,F2 6768 | A,F1,F2 | -            | A       | -      |

<sup>a</sup>For GXXXL(B) grating tests, the grating settings are the default central wavelengths. For GXXXM(B) the grating settings are listed as the central wavelength in Å. A = star in slit. F1 = star behind fiducial F1 (0.5/arcsec). F2 = star behind fiducial F2 (0.8/arcsec)

Exposure times, which are not listed, were selected to keep the recorded spectra significantly below the 32,000 DN levels with the CCD GAIN=4. Where the fluxes were significantly lower, GAIN=1 was used to keep above video pickup levels close to the star. As the desired dynamic range is quite large, we rapidly reach flux levels affected by detector noise, cosmic ray events and even bias shifts across the CCD columns. Indeed some LSF plots exhibit a pronounced asymmetry from below the star in the spatial direction to above the star. This is a known bias shift problem. Correcting for it is not a simple matter. We chose to not correct for the shift as a means of cautioning the observer that it is there.

The line spread functions are presented in figures 2, 9–13. This are averaged LSFs for the selected grating. Each spectrum is precisely aligned using WAVECAL lamp spectra and the trace of the stellar spectrum, or the illuminated edges of the fiducial, when the star is blocked by the fiducial, F1 or F2. Again, we caution the reader that these LSFs are collapsed along the spectral dispersion (re-sampled row) direction. For the G750L spectra, the average is taken from 5000Å to 10,000Å, and is greatly affected by the CCD scatter in the reddest portion of the spectrum, especially beyond 7000Å. Proper corrections would require a wavelength-dependent LSF from 5000 to 10,000Å. For contrasts up to  $10^3$ , the current data may be sufficient, but the proper scatter function must have the wavelength dependency included. For Figure 2, and for Figures 9–13, the flux along the spatial (cross-dispersion) axis is logarithmic ranging from  $10^0$  to  $10^{-8}$ . Each CCD pixel subtends 0.0504".

These plots extend from approximately  $10''$  below to  $10''$  above the star, which is centered near row 512.

The top trace is of the star centered in the  $52'' \times 0''.2$  aperture and is normalized to the total measured flux. The LSF drops slowly, but symmetrically, from the stellar peak. At  $10''$  distance from the star the detected flux is  $\sim 10^{-4}$  of the total flux. The central trace describes the LSF when the star is placed behind the F1 ( $0''.5$ ) fiducial. The scattered light at the position of the star drops by  $10^4$ , and the off-axis scattered light drops by a factor of  $10^2$ . The bottom trace describes the LSF when the star is placed behind the F2 ( $0''.8$ ) fiducial. The scattered light is not affected significantly in the innermost few arcseconds, but at  $\sim 10''$ , the scattered light is decreased by a factor of two compared to the scattered light from the F1 fiducial measurement.

The shoulder, visible to the left of the unobscured stellar peak, is the ghost that we discussed above (Figures 3-6). Placing the star behind either fiducial drops this shoulder as expected. However, the light that passes the fiducial, diffracted and scattered light from the telescope, still produces ghosts. As the signal/noise is excellent, we can see the fainter ghost due to the left edge of the fiducial for F1 and even for F2. The ghost for the right hand portion of the light passing the fiducial contributes to filling in the area subtended by the fiducial and contributes to the flux on the left hand side of the fiducial. If the star and the fiducial-blocked star were centered on row 100, the ghost would shift in the y-direction to above the star and fiducials.

In the following section, we will be intercomparing the LSF's for the different grating combinations and spectral types. Since these plots were originally done in color, the three traces are not easily separated in the black and white version. However, the star in the aperture is always the top curve, the intermediate curve is the F1 fiducial and the bottom curve is the F2 fiducial; the performance of the fiducials is consistent. We also note that these fiducials were moved in and out without re-centering the star. The astrometry was remarkable as demonstrated by the symmetry of the stellar core and the scattered light on both sides of the fiducials. Indeed, the success of proposal 8844 is good evidence to extend support to these other three fiducials.

## 5. LSF Intercomparisons

Figure 9 shows the collapsed LSF's for the three coronagraphic reference stars of spectral types AOV, GV, MIII. As these are the averaged LSF's from 5000 to 10,000Å, the LSF has variations determined by the CCD response to the specific star's spectral distribution. Little difference is noted between the star-in-aperture LSFs. The most significant difference is when the star is behind the F2 fiducial. The LSF of the AOV star (lower left) appears to drop off relatively sharply. Indeed, this LSF, which should be weighted towards 5000Å more than towards 10,000Å, is similar to the spectral LSF measured over the narrow spectral interval by the G750M grating (upper left) centered at 6768Å.

Figure 10 compares the LSFs for HD114653 (AOV) for the G750L and selected G750M settings. The G750M (8561Å) LSF (lower left) is noticeably similar to the G750L LSF (upper left), other than S/N. The G750M (6768Å) LSF (upper right) wings drop off faster for the F1 fiducial than the LSF centered on 8561Å (the F2 fiducial measure was dropped due to observing constraints). The G750M (6768Å) grating setting was observed with both the  $52'' \times 0''.2$  aperture and the  $52'' \times 0.1$  aperture. Little difference, other than S/N is noted.

Figure 11 plots the G430L LSFs for all four program stars. As would be expected, the scattering drops off much faster than the G750L LSFs, since the telescope optics diffraction pattern gets sharper and the CCD silicon layer is optically much thicker. The visible-wavelength photons do not penetrate very deep before detection. By contrast, CCD is nearly transparent to the photons near 10,000Å and the diffraction pattern drops half as quickly. The G430M LSFs produced by the four stars are quite similar: the diffraction

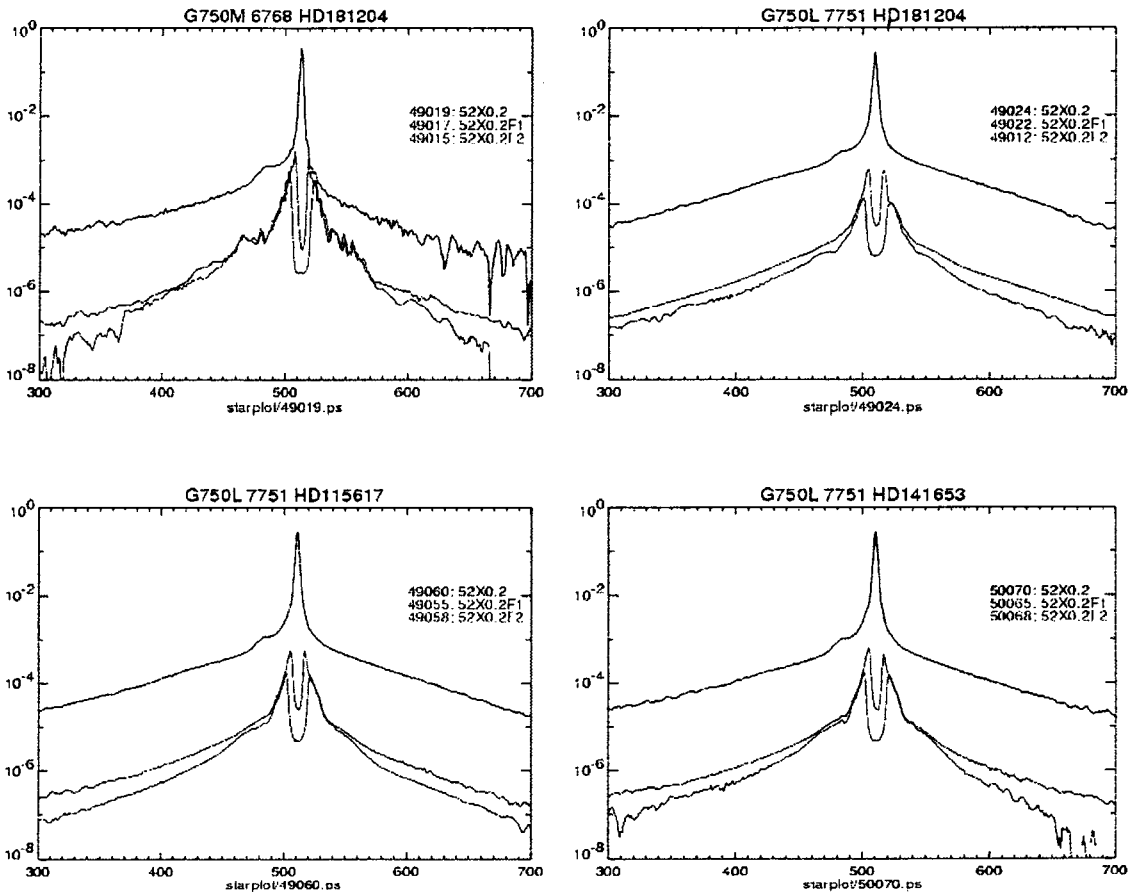


Figure 9. Comparison of LSF for G750L for HD181204 (MIII, upper right), HD115617 (GV, lower left), and HD141653(A0, lower right). Upper left is the LSF for G750M for HD181204(MIII) centered at 6768Å

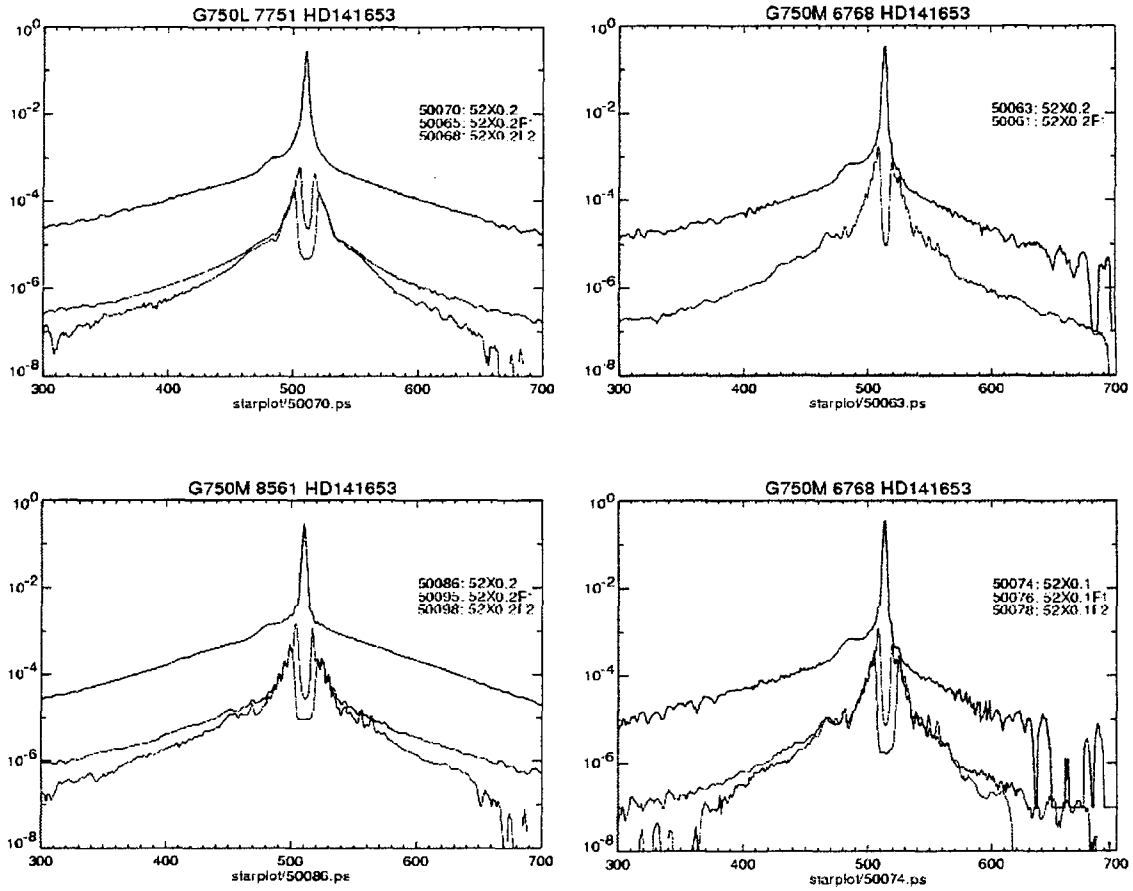


Figure 10. Comparison of LSFs for HD114653 (GV) Upper left: G750L Lower left: G750M centered at 8561Å Upper right: G750M centered at 6768Å tested with 52"x0.2" aperture. Lower right: G750M centered at 6768Å tested with 52"x 0.1" aperture.

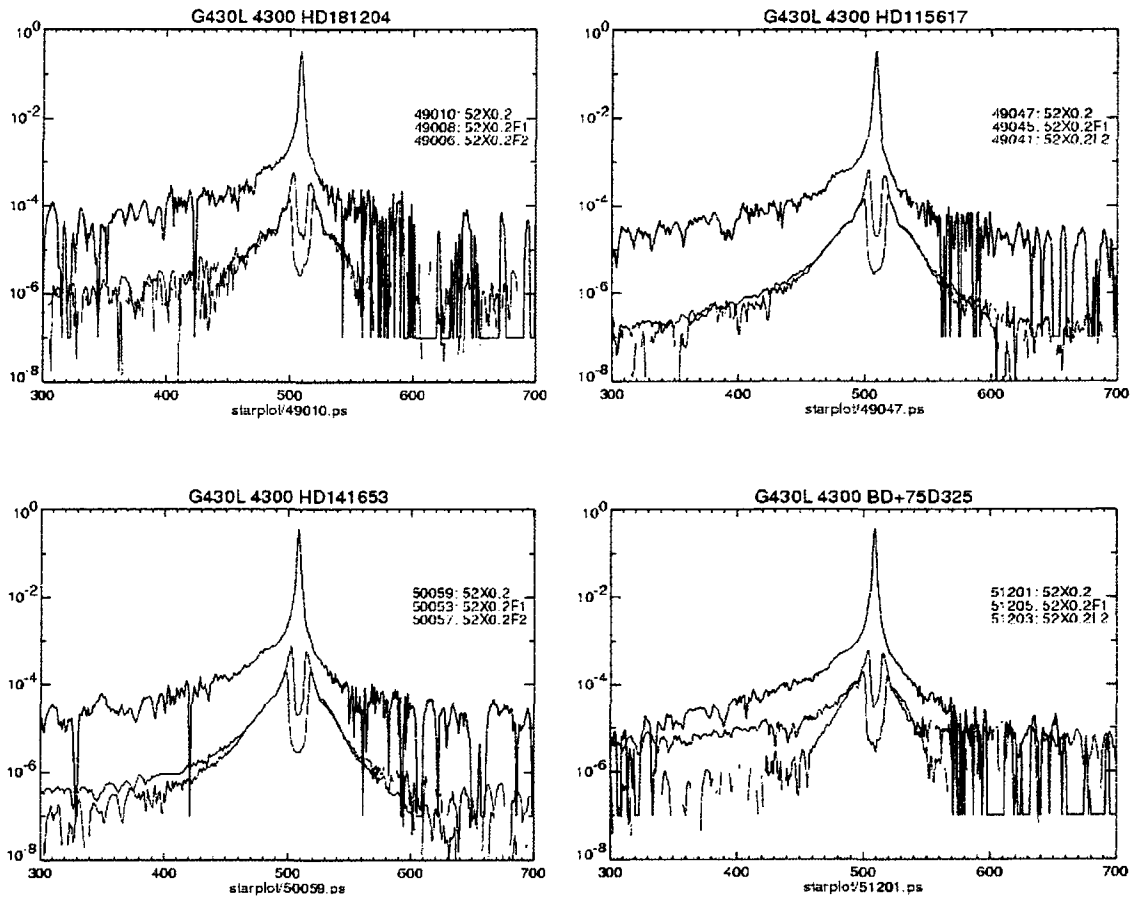


Figure 11. G430L comparisons for all four stars

pattern is close to the core of the star; the ghost is easily seen on the left shoulder; and the bias level becomes a significant variable between the lower rows and the upper rows of the CCD. Figure 12 plots the three measures of the G430M LSFs in comparison to the G430L LSF. S/N becomes an even more difficult issue for these spectra as the scattered/diffracted light drops down to levels only marginally detectable with 32000 DN encoding. The bias level also is a problem. Indeed BD+75D325 LSF measures are strongly limited by the detector background. One peculiarity is that the ghost signal appears stronger for the G430M (4961Å) setting than for the 3936Å setting. This is likely due to the antireflection coating applied to the window to enhance the blue sensitivity.

While several LSFs were measured for the G230LB and G230MB gratings, the LSFs differ only in S/N. Figure 13 shows only the LSF measures for BD+75D325 as they are the ones with the best S/N. They appear well-behaved and indeed the ghost on the shoulder is significantly weaker than for spectra to the red. The wings in all three LSFs are limited by the finite DN range from the CCD. It is tempting to combine the three LSFs into one as the F1 and F2 fiducial LSFs nestle so well with the star in the aperture. This suggests that indeed the fiducials would be useful to block starlight in the G230LB and G230MB modes as they primarily attenuate the core of the telescope PSF and STIS with CCD does not contribute a significant scatter component, unlike the G750L and G750M portions of the spectra.

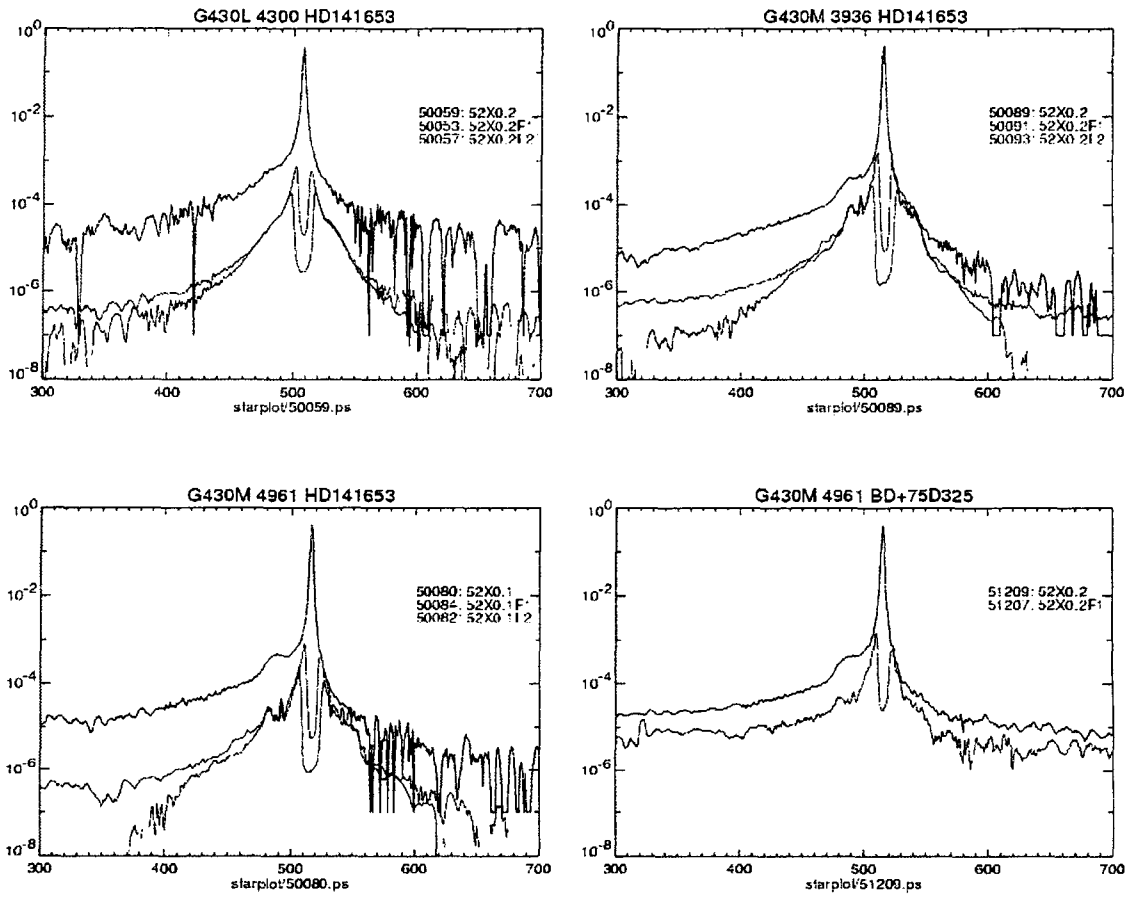


Figure 12. G430L and G430M comparisons for A0V HD141653 and WD BD75+325

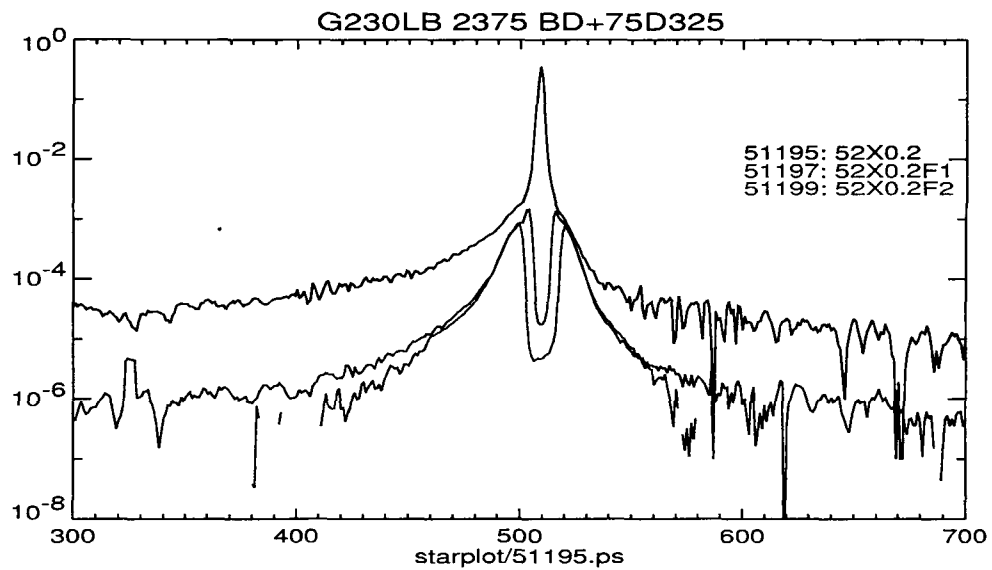


Figure 13. G230L LSF comparisons for WD BD75+325

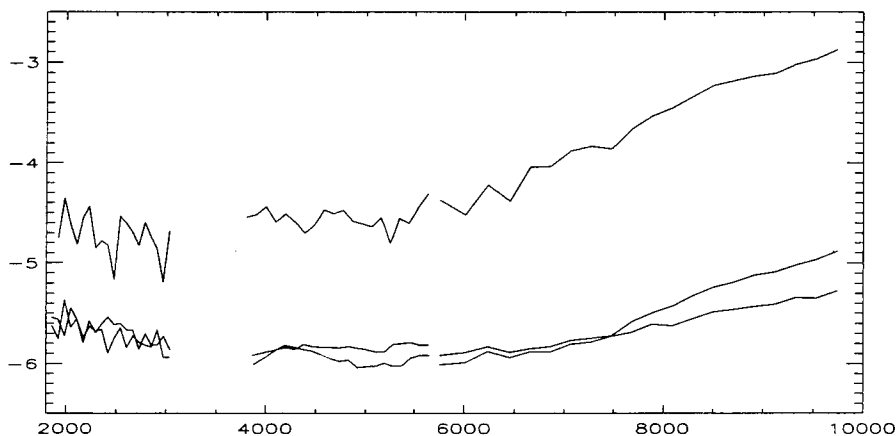


Figure 14. The Measured Scattered Light Component as a Function of Wavelength at a Position Offset  $3''$  from the Star Position in the positive spatial (cross dispersion) direction on the CCD. The abscissa scales the scattered light as  $\text{alog}_{10}(\text{flux})$  relative to the peak flux of the star being unity. Top curve is a measure of the scattered light when the star is centered within the STIS  $52'' \times 0''.2$  aperture. The bottom two curves, which are not separable below  $7000\text{\AA}$ , are measures of the scattered light when the star is positioned behind the F1 fiducial and then the F2 fiducial. Relative fluxes below  $6000\text{\AA}$  should be considered upper limits to the scatter as in all three curves, the digitization level, video pickup, bias levels, dark current and cosmic ray contributions are comparable.

Figure 14 brings together the contribution to the background as a function of wavelength for an angular displacement offset by three arcseconds from the star in the  $+Y$ -direction. The three curves are for the star in the aperture, behind the F1 fiducial and then behind the F2 fiducial. Compared to the total flux being unity, the scattered/diffracted starlight contribution is below a few parts in  $10^5$  from 2000 to  $6000\text{\AA}$ . Longward of  $6000\text{\AA}$  the scattered light component becomes noticeable, primarily due to scatter in the STIS CCD and climbs to a level of  $\sim 10^{-3}$  at  $10,000\text{\AA}$ . With the star placed behind either fiducial, the scattered component drops 100-fold at  $10,000\text{\AA}$  and is below  $10^{-6}$  shortward of  $7000\text{\AA}$ . The rise in scattered light shortward of  $3000\text{\AA}$  is consistent with measured HST light scatter due to roughness of the mirror surface.

Finally we wish to point out that the *LSF* measures in this discussion are really a linear approximation to a scattering phenomenon that must radially transmit through the CCD chip in a fairly random pattern. This pattern will depend on the details of the CCD fabrication: how thick and uniform is each layer of etched circuitry and the uniformity of sensitivity. From Malumuth et al. (2002) we learned that the CCD chip is wedge-shaped and that the sensitivity fringes are distorted by this apparent shape. A proper model of the detected scattered light would also have to take into account the smoked support glass that supports the CCD chip within the housing, necessary to help the CCD survive during the launch vibrations.

## 6. Conclusions

This discussion describes a first pass at quantifying the instrumental scatter of STIS in combination with HST. We observed four stars ranging from a WD to MIII in spectral type,

working in coordination with coronagraphic observers. Future work is intended to define a tool for subtracting the ghost feature, and possibly defining a wavelength-dependent LSF.

**Acknowledgments.** We are grateful to the Space Telescope Science Institute STIS Team, their contribution of observing time and positive encouragement in reducing and interpreting the data. One of us (Don Tennant), as a volunteer summer student from the United States Naval Academy, provided much of the data reduction used in this paper. We acknowledge the very helpful support of Mr. Keith Feggans in the preparation of the figures for this publication.

## References

- Hill, R. S. STIS Postlaunch Quick Look Reports 63 and 65  
*[http://hires.gsfc.nasa.gov/stis/postcal/quick\\_reports/quick\\_reports.html](http://hires.gsfc.nasa.gov/stis/postcal/quick_reports/quick_reports.html)*
- Ishibashi, K. et al. 2002, AJ, submitted
- Malumuth, E., et al. 2002, PASP, accepted
- Rubin, R., et al. 2001 MNRAS, 334, 777
- Zethson, T. 2000 PhD Dissertation, Lund University, Sweden
- Zethson, T., Gull, T., et al. 2000 AJ, 12, 34